Subsurface Reconstruction From GPR Data by 1-D DBIM and RTM in Frequency Domain

Junping Xiao, Xi Tang, Bingyang Liang, Feng Han, *Member, IEEE*,
Hai Liu, *Member, IEEE*, and Qing Huo Liu, *Fellow, IEEE*

***Abstract*— This letter presents the joint reconstruction of unknown subsurface structures by the full-wave inversion (FWI) and reverse time migration (RTM) imaging. In the FWI, the 1-D distorted Born iteration method (DBIM) is employed to retrieve the dielectric parameters of the layered subsurface medium by minimizing the difference between measured fields and calculated fields via Fréchet derivatives. Based on the inversion results, the RTM is directly performed in the frequency domain to image the buried objects using the ground-penetrating radar (GPR) data. Numerical and laboratory experiments show that the proposed joint method can be used to reconstruct the subsurface structures reliably and efficiently.**

***Index Terms*— 1-D distorted born iteration method (1-D DBIM), ground-penetrating radar (GPR), reverse time migration (RTM).**

I. INTRODUCTION

REVERSE time migration (RTM) is usually recognized as superior to other migration algorithms in imaging accuracy. It is to extrapolate the source wavefields and the time-reversed receiver wavefields, and then overlap the imaging result of each shot to obtain the final imaging profile [1]. RTM has been widely applied to seismic exploration [2], image reconstruction for optical tomography [3], complex sea anisotropic imaging [4], and reflectivity map reconstruction in subsurface layered media by borehole radars [5]. The traditional RTM is performed by finite-difference time domain (FDTD) method to calculate the forward and backward wavefield extrapolation [6], and has been improved to accommodate lossy and dispersive media [7]. The recently proposed RTM in the frequency domain (FRTM) has the tremendous computation speed advantage over RTM in the time domain (TRTM) when the subsurface structure is horizontally layered [8]. The reason is that the layered medium dyadic Green's functions (DGFs) are computed in advance and saved, and directly loaded when RTM is performed. However, no matter for TRTM or FRTM, the result is sensitive to the input of the velocity model of the background medium [9], which is mainly determined by the dielectric parameter and thickness of each layer. An inaccurate initial velocity model of the background medium can cause position shift or shape distortion of the buried object image [10], [11].

Several inversion methods have been proposed to determine the background dielectric parameters in ground-penetrating radar (GPR) applications. They mainly include the travel-time measurement [12]–[14]; full-wave inversion (FWI) in the time domain [15], [16], in the frequency domain [17], as well as in the spectral domain [18]; and the plane-wave approximation of FWI [19], [20], which can achieve the same computation accuracy as FWI but runs much faster. In this letter, we use a fast but rigorous 1-D FWI, the distorted Born iteration method (DBIM), to invert for the unknown dielectric parameters of the layered subsurface medium first, and then combine the obtained model parameters with the FRTM algorithm to reconstruct the buried objects. Both the DBIM and FRTM are performed in the frequency domain. We first validate the proposed method by numerical simulated GPR data and then conduct an experiment in a sandpit in the laboratory to further verify the accuracy and feasibility of the method.

This letter is organized as follows. In Section II, we introduce the procedure of the FRTM and DBIM inversion of dielectric constants. In Section III, we present the implementation of our algorithm in a simulation model. In Section IV, a laboratory experiment is conducted to demonstrate the feasibility of the algorithm in practical engineering applications. Finally, we make conclusion and future remarks in Section V.

II. THEORY

One of the common velocity models used for RTM of real GPR data is the horizontally layered structure. In such a scenario, electromagnetic (EM) waves collected by receivers include direct coupling from transmitters, reflected waves from layer boundaries, and scattered waves from buried objects. The model parameters of unknown layered background media include ϵ_n, σ_n, and d_n, which represent permittivity, conductivity, and vertical depth of the nth layer, respectively. In this letter, the dispersion of the underground medium is not considered. Thus, ϵ_n in each layer has no variation with frequency. The conductivity is mainly caused by moisture. However,

---

Manuscript received January 7, 2019; revised May 31, 2019; accepted July 7, 2019. Date of publication July 24, 2019; date of current version March 25, 2020. This work was supported by the National Natural Science Foundation of China under Grant 41504120. *(Corresponding author: Feng Han.)*

J. Xiao, X. Tang, B. Liang, and F. Han are with Institute of Electromagnetics and Acoustics and Key Laboratory of Electromagnetic Wave Science and Detection Technology, Xiamen University, Xiamen 361005, China (e-mail: feng.han@xmu.edu.cn).

H. Liu is with the School of Civil Engineer, Guangzhou University, Guangdong 510006, China (e-mail: hliu@gzhu.edu.cn).

Q. H. Liu is with the Department of Electrical and Computer Engineering, Duke University, Durham, NC 27708 USA (e-mail: qhliu@duke.edu).

Color versions of one or more of the figures in this letter are available online at http://ieeexplore.ieee.org.

Digital Object Identifier 10.1109/LGRS.2019.2927638

numerical simulations show that the effects of conductivity on the retrieved permittivity of each subsurface layer and the RTM of GPR data are negligible if its value is in the order or less than 1 mS/m. Therefore, we set the conductivity less than 1 mS/m and only retrieve two sets of unknowns ϵ_n and d_n in this letter. In both simulations and laboratory experiments, we designed similar models to verify the method.

A. FRTM Imaging

The detailed procedure of FRTM was presented in our previous work [8]. The basic idea is to directly perform summation of all the wavefields in the frequency domain. The image condition is compactly written as

$$I(\mathbf{r}) = \frac{1}{2\pi}\int_{-\infty}^{+\infty} U_s(\mathbf{r},\omega)U_r(\mathbf{r},\omega)e^{j\omega T}dw \tag{1}$$

where $U_s(\mathbf{r},\omega)$ and $U_r(\mathbf{r},\omega)$ are the Fourier spectra of the source wavefield and the receiver wavefield, respectively. $\mathbf{r}$ is the spatial sampling position in the imaging domain, T is the time window of the recorded GPR traces, and ω is the angular frequency. $\mathbf{U}_s(\mathbf{r},\omega)$ and $\mathbf{U}_r(\mathbf{r},\omega)$ are computed by multiplying DGFs with the corresponding spectra of source wavelet and receiver signals [8]

$$\mathbf{U}_s(\mathbf{r},\omega) = \overline{\overline{\mathbf{G}}}(\mathbf{r},\mathbf{r}_s,\omega)\cdot\mathbf{S}(\mathbf{r}_s,\omega) \tag{2}$$

$$\mathbf{U}_r(\mathbf{r},\omega) = \overline{\overline{\mathbf{G}}}(\mathbf{r},\mathbf{r}_r,\omega)\cdot\mathbf{R}^*(\mathbf{r}_r,\omega)e^{-j\omega T} \tag{3}$$

where $\overline{\overline{\mathbf{G}}}$ is the DGF. $\mathbf{S}(\mathbf{r}_s,\omega)$ and $\mathbf{R}(\mathbf{r}_r,\omega)$ are the spectra of the source waveforms excited at the source location $\mathbf{r}_s$ and the recorded signals at the receiver location $\mathbf{r}_r$, respectively. The superscript * represents the complex conjugate. When FRTM is implemented, DGFs are directly loaded to improve the computation efficiency. However, $\overline{\overline{\mathbf{G}}}$ depends on the dielectric parameters and layer configuration of the subsurface medium. Therefore, they must be evaluated first.

B. Dielectric Parameter Inversion

In our previous work [21], 1-D DBIM has been successfully used to invert for the conductivity of the layered underground structure from grounded electrical-source airborne transient EM (GREATEM) data. In this letter, we take the similar procedure but use the 1-D DBIM to invert for the permittivity of the layered subsurface structure from GPR data. In the forward modeling, we use the Fréchet derivative to calculate the EM response at the receivers on account of a small perturbation of the permittivity in a certain layer of the subsurface medium. Maxwell's equations with an electric current source are given as

$$\nabla\times\mathbf{E} = -j\omega\mu_0\mathbf{H} \tag{4}$$

$$\nabla\times\mathbf{H} = j\omega\varepsilon\mathbf{E}+\mathbf{J} \tag{5}$$

where ε is the unknown dielectric constant. The dipole antenna source is expressed as

$$\mathbf{J} = \mathbf{I}l\delta(\mathbf{r}-\mathbf{r}') \tag{6}$$

where $\mathbf{I}l$ represents the electric dipole moment. Assume that a small perturbation $\delta\varepsilon_{\mathrm{n}}$ is generated for the permittivity of the nth layer. By substituting the small perturbation into (4) and (5), we obtain the field perturbation equation as

$$\nabla\times\delta\mathbf{E}(\mathbf{r}_r,\mathbf{r}_s) = -j\omega\mu_0\delta\mathbf{H}(\mathbf{r}_r,\mathbf{r}_s) \tag{7}$$

$$\nabla\times\delta\mathbf{H}(\mathbf{r}_r,\mathbf{r}_s) = j\omega\varepsilon\delta\mathbf{E}(\mathbf{r}_r,\mathbf{r}_s)+\mathbf{J}'(\mathbf{r}) \tag{8}$$

where $\mathbf{J}'(\mathbf{r}) = j\omega\delta\varepsilon_n\mathbf{E}$ is treated as the equivalent source, $\mathbf{r}_r$ and $\mathbf{r}_s$ are the receiver and source locations, respectively, and $\mathbf{r}$ represents a location in the perturbed layer. A matrix linking the perturbation $\delta\varepsilon$ in each layer and the field perturbation at receivers is the Fréchet derivative matrix $\mathbf{F}$ [21].

In the inversion, we retrieve the permittivity of each layer from the measured fields at receivers. The cost function for DBIM is defined as

$$\mathrm{C}(\delta\boldsymbol{\varepsilon}_{m+1}) = \frac{\|\delta\mathbf{f}-\mathbf{F}\cdot\delta\boldsymbol{\varepsilon}_{m+1}\|^2}{\|\mathbf{f}^{\mathrm{mea}}\|^2}+\gamma^2\frac{\|\delta\boldsymbol{\varepsilon}_{m+1}\|^2}{\|\boldsymbol{\varepsilon}_m\|^2} \tag{9}$$

where $\|\cdot\|$ represent the L_2-norm, $\mathbf{f}^{\mathrm{mea}}$ is the measured field, $\delta\mathbf{f}$ denotes the difference between the measured and predicted fields, $\mathbf{F}$ is the Fréchet derivative matrix, $\mathbf{F}\cdot\delta\boldsymbol{\varepsilon}_{m+1}$ represents the field variation caused by the permittivity vector update $\delta\boldsymbol{\varepsilon}$ in the $(m+1)$th iteration, and γ is a regularization factor. Minimization of (9) is equivalent to solving the following equation [22]:

$$\left(\frac{\mathbf{F}^*\mathbf{F}}{\|\mathbf{f}^{\mathrm{mea}}\|^2}+\frac{\gamma^2}{\|\boldsymbol{\varepsilon}_m\|^2}\right)\delta\boldsymbol{\varepsilon}_{m+1} = \frac{\mathbf{F}^*\delta\mathbf{f}}{\|\mathbf{f}^{\mathrm{mea}}\|^2} \tag{10}$$

where the $\mathbf{F}^*$ represents the conjugate transpose of $\mathbf{F}$. In this letter, we use the conjugate gradient (CG) method to solve (10) iteratively. The flowchart of the entire DBIM procedure is given in [21]. We also define the relative error of the retrieved permittivity of the background medium as

$$\mathrm{err} = \frac{\|\boldsymbol{\varepsilon}^r-\boldsymbol{\varepsilon}\|}{\|\boldsymbol{\varepsilon}^r\|} \tag{11}$$

where $\boldsymbol{\varepsilon}^r$ and $\boldsymbol{\varepsilon}$ are the retrieved and true permittivity vector, respectively. We keep updating $\boldsymbol{\varepsilon}^r$ to minimize the cost function and obtain the best result.

III. NUMERICAL RESULTS

In this section, we design a numerical model to demonstrate the effectiveness and accuracy of the proposed algorithm. As shown in Fig. 1(a), there are two layers underground, with the relative permittivity $\varepsilon_{r2} = 2.2$ and $\varepsilon_{r3} = 4.8$, respectively. Their conductivity is set as 1 mS/m. The layer boundary is located at $z = 0.25$ m. A metal sphere with the radius of 7 cm and a plastic sphere with a radius of 6 cm are buried in the subsurface region. We perform three sets of numerical simulations to investigate how the depth of the buried objects and their horizontal distance affect the proposed joint method. The depths of two spheres are set as $d_v = 0.105$, 0.22, and 0.35 m, respectively. In each set of numerical experiments, the distance d_h between two spheres changes from 0.13 to 0.85 m with an interval of 0.08 m. The GPR data are simulated with a pair of dipole antennas with the common-offset (CO) of 10 and placed 20 cm above the ground surface. The source wavelet is the Blackman–Harris window (BHW) function with the center frequency of 1.4 GHz. The CO GPR profiles

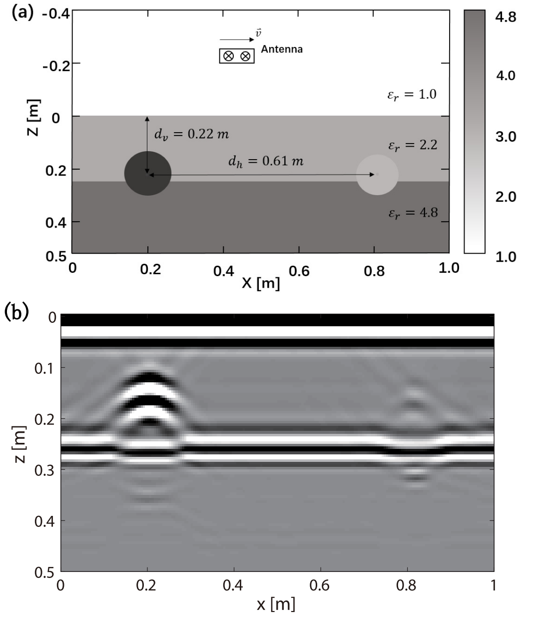

Fig. 1. Simulation model with two subsurface layers. The dipole antenna moves 20 cm over the ground. (a) Simulation model. (b) Imaging result. Only the configuration and RTM result for $d_v = 0.22$ m and $d_h = 0.61$ m are illustrated.

contain 141 traces with a step of 1 cm. All the simulations are performed using a commercial FDTD simulation software.

In the inversion process, we first reconstruct the dielectric parameters of subsurface layers and then perform FRTM to reconstruct the subsurface image. Besides the two unknowns ε_{r2} and ε_{r3}, the boundary position between the second and third layers is also unknown. Unfortunately, the 1-D DBIM algorithm proposed in Section II-B can only retrieve the dielectric constants in each layer when the layer boundaries are known. Therefore, we try different layer boundary positions z to minimize the cost function (9). Let

$$z = z_0 + (n-1)\triangle d \tag{12}$$

where z_0 is the beginning value of z, $\triangle d$ is the increment step in each trial, and n is an integer number used for calculating the variate z during the iteration. In our numerical experiment, $z_0 = 1.2$ mm and $\triangle d = 1.2$ mm. In each trial, we use simulated electric field data at 11 spatially uniform positions and seven sampling frequencies from 0.9 to 1.5 GHz with the step of 0.1 GHz. Therefore, 77 sets of data are used in each inversion. Fig. 2 shows how the depth d_v of two spheres and the distance d_h between two spheres affect the reconstructed layered subsurface permittivity. As we can see, smaller d_v leads to a larger error that is mainly contributed by the retrieved permittivity of the second subsurface layer. The effect of d_h is negligible. The scattered waves from two spheres become stronger when d_v is smaller. They interfere with the reflected waves from subsurface layer boundaries and increase the reconstruction error. However, the reflected waves from the first subsurface layer are strong enough and thus almost not affected by scattered waves from two spheres. In addition, because the simulated data used for reconstruction are provided by an antenna array with the size larger than 1 m, the change of d_v less than 1 m has a negligible effect.

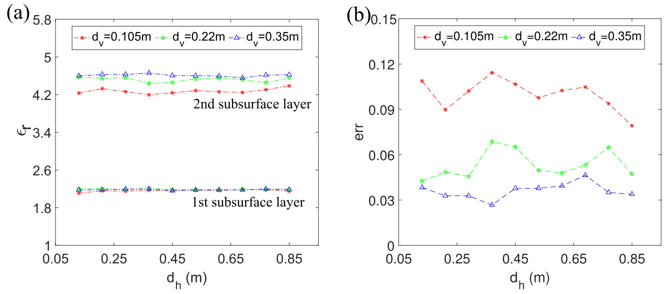

Fig. 2. Effects of d_v and d_h on the retrieved relative permittivity. (a) Relative permittivity for different d_v and d_h values. (b) Error defined in (11) for different d_v and d_h values.

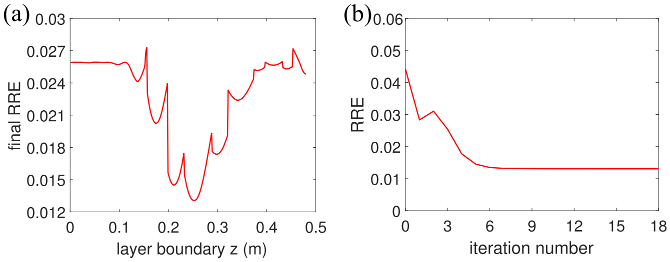

Fig. 3. Variations of the RREs between the simulated fields and the predicted values in the inversion processes. (a) Final RREs for different z values. (b) Converge curve for the z value when the final RRE in (a) is minimum.

Then, we choose $d_v = 0.22$ m and $d_h = 0.61$ m to investigate the DBIM convergence process. Totally, we made 400 trials for (12). The final relative residual errors (RREs) between calculated electric fields and simulated electric fields when the CG iterations stop are shown in Fig. 3(a). We can see that the residual error reaches the minimum value when $z = 0.2520$ m. Compared with the true position of the boundary at $z = 0.25$ m between the second and third layers, the reconstructed z value is very close with a relative error of 0.8%. Fig. 3(b) shows the residual error variation versus the iteration number in the trial for $z = 0.2520$ m. The iteration converges fast in the first five steps and then the residual error decreases slowly. The final residual error keeps around 1.3%.

The reconstructed relative permittivities ε_{r2} and ε_{r3} when $z = 0.2520$ m are 2.178 and 4.548, respectively. Compared with the true values of 2.2 and 4.8, the relative error defined in (11) is 4.79%. Based on these reconstructed model parameters, we carry out the FRTM imaging and the result is shown in Fig. 1(b). Since the FRTM is based on layered-medium DGFs, we only computed the DGFs for underground layers, and thus, only the underground structures are imaged. The boundary position between the second and third layers in the image is approximately 0.25 m, close to the real position. In addition, the position of the top surface of the metal sphere is near 0.15 m, which is the true position. The bottom surfaces of the two spheres are also visible in the image. Therefore, in the numerical simulation, we can accurately reconstruct the dielectric parameters and the layer boundary position of a two-layer subsurface medium and then use the retrieved parameters to build the model and reconstruct the buried object with FRTM.

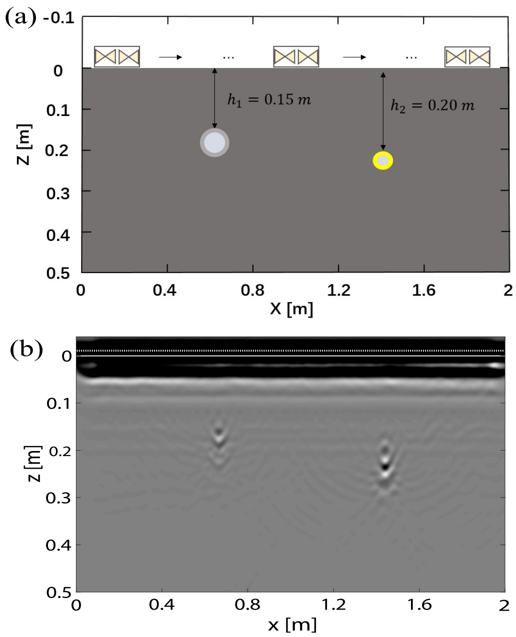

Fig. 4. Experimental model with two layers. The IDS antennas are placed 2 cm over the sandpit. (a) Experimental model. (b) Imaging result.

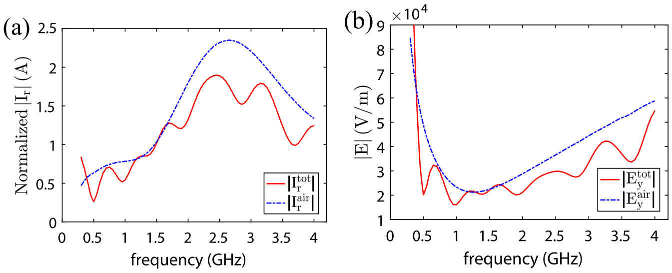

Fig. 5. (a) Normalized measured I_r and (b) calculated E_y spectra for the measurement right above the metal pipe buried in sandpit.

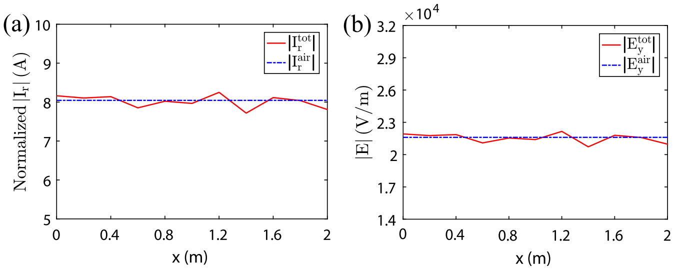

Fig. 6. (a) Normalized measured I_r and (b) calculated E_y in 11 spatially uniform sampling positions over the sandpit when the operation frequency is 1150 MHz.

IV. LABORATORY EXPERIMENT

A laboratory experiment is presented in this section. As shown in Fig. 4(a), we conducted our experiment over a sandpit and collected a CO GPR profile containing 201 traces with a step of 1 cm via a commercial GPR system. The IDS antennas are used and the distance between the transmitting and receiving antennas is about 4 cm. They are polarized in the $\hat{y}$-direction, and move in the $\hat{x}$-direction, as shown in Fig. 4(a). The IDS antenna works with a center frequency of 1.6 GHz and moves around 1 cm over the sand surface. An air-filled plastic pipe with a diameter of z cm and a metal pipe with a diameter of 3 cm are buried in the sandpit. The top surfaces of the two pipes are around 15 and 20 cm from the sand surface, respectively, as shown in Fig. 4(a). The dielectric parameters of the sand are given in [8]. In this experimental model, there is only one unknown layer, the sand. Therefore, we only need to retrieve one parameter by using the DBIM before performing the FRTM.

In the 1-D inversion, we use EM waves radiated by an infinitesimal electrical dipole and reflected by the underground layered media to reconstruct the dielectric constants. However, the output data from the IDS antenna feed port are current instead of electric fields. Therefore, the measured current data cannot be directly used to perform 1-D DBIM inversion. To resolve this issue, we adopt the method proposed in [23]. It is assumed that the current signals at the antenna feed port are proportional to the co-polarized electric fields excited or received by a unit dipole source in the frequency domain. This is valid for the data collected in the low-frequency range in our experiment. In this way, we have

$$I_r^{\text{air}} = C_0 \hat{y} \cdot \mathbf{E}^{\text{air}}(\mathbf{r}_r, \mathbf{r}_s) \tag{13}$$

and

$$I_r^{\text{tot}} = C_0 \hat{y} \cdot \mathbf{E}^{\text{tot}}(\mathbf{r}_r, \mathbf{r}_s) \tag{14}$$

where I_r^{air} represents the measured antenna port current in the air when the underground layered structures are absent, while I_r^{tot} is the measured current when the underground layered structures are present. $\mathbf{E}^{\text{air}}$ and $\mathbf{E}^{\text{tot}}$ denote the electric fields excited by unit dipoles in the aforementioned two scenarios, respectively. C_0 is a frequency-dependent constant, which represents the ratio of current to electric field. Before inversion, we can acquire $\mathbf{E}^{\text{air}}$ by analytical calculation, and then $\mathbf{E}_y^{\text{tot}}$ is obtained by

$$\mathrm{E}_y^{\text{tot}}(\mathbf{r}_r, \mathbf{r}_s) = \frac{I_r^{\text{tot}} \cdot \mathrm{E}_y^{\text{air}}(\mathbf{r}_r, \mathbf{r}_s)}{I_r^{\text{air}}} \tag{15}$$

which will be used as the measured field data to perform the DBIM inversion.

Fig. 5(a) and (b) shows the normalized magnitudes of measured I_r spectra right above the buried metal pipe and the corresponding calculated E_y. We can see that the difference shown for the measured current when the sand is absent and present is appropriately reflected in the electric fields. In this letter, we use the measured data when the operation frequency is lower than 1.2 GHz since the IDS antenna behaves more like a dipole antenna in the lower frequency band. On the other hand, the magnitude variations of E_y and I_r versus 11 spatially uniform sampling positions over the sandpit for the frequency 1150 MHz are shown in Fig. 6. We can see that the variations in the total current and electric fields in different positions are not very sharp, which are actually caused by the CO GPR measurement. In the inversion, we use data sampled at these 11 positions for two sampling frequencies, 500 and 1150 MHz. Therefore, there are totally 22 sets of measured data used in the inversion.

Fig. 7 shows the convergence curve of DBIM when E_y^{tot} from (15) are used as the measured data. After around three iterations, the RRE approaches 6.6% and keeps almost

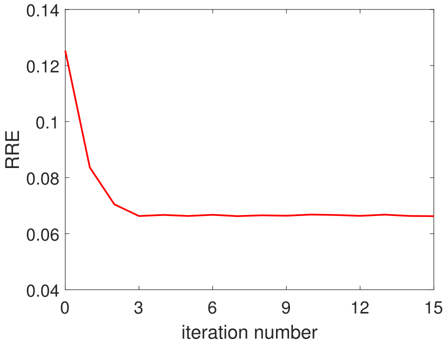

Fig. 7. RREs of the computed total fields compared with the measured data versus the number of iterations.

unchanged. The retrieved relative permittivity is 3.2, which is a little larger than the true value 3.0 of dry sand. Fig. 4(b) shows the FRTM imaging result based on the retrieved permittivity. The buried plastic pipe and the metal pipe are clearly imaged, and they are around 0.15 and 0.2 m from the sandpit surface, respectively, which are consistent with the true positions.

V. CONCLUSION

In this letter, the 1-D DBIM and FRTM are combined to reconstruct the layered subsurface medium parameters as well as the buried object images. The FWI method DBIM and RTM in the frequency domain are jointly applied to the GPR data. The 1-D DBIM was originally proposed to reconstruct the conductivity of the underground layered medium and is modified slightly in this letter to determine the background permittivity for FRTM imaging. To verify the accuracy and reliability of the proposed joint algorithm, we not only perform numerical tests but also conduct a laboratory experiment in a sandpit. Although the subsurface layer boundary position is determined by a series of trials in the numerical experiment, the result is precise and the reconstructed subsurface structure is close to the true scenario. In the laboratory experiment, the subsurface medium is homogeneous, and the electric fields are obtained by assuming that they are proportional to the measured current in the antenna feed ports in the low-frequency range.

Although this is the first attempt to combine the 1-D FWI DBIM with FRTM, the reliable reconstructed results in both the numerical and laboratory experiments imply the potential applications of the proposed joint method for subsurface detection. The future work will be focused on two aspects: 1) improve the 1-D DBIM to invert for both the layer positions and dielectric parameters and 2) improve the FRTM to reconstruct buried objects in a circumstance with large conductivity to account for high moisture. A heuristic work has been accomplished in [24] but in the time domain. We will perform the loss compensation in the frequency domain.

REFERENCES

[1] J. Zhu and L. R. Lines, "Comparison of Kirchhoff and reverse-time migration methods with applications to prestack depth imaging of complex structures," *Geophysics*, vol. 63, no. 4, pp. 1166–1176, May 1998.

[2] Y. Chen, J. Yuan, S. Zu, S. Qu, and S. Gan, "Seismic imaging of simultaneous-source data using constrained least-squares reverse time migration," *J. Appl. Geophys.*, vol. 144, pp. 32–35, Mar. 2015.

[3] Z. Wang, H. Ding, G. Lu, and X. Bi, "Reverse-time migration based optical imaging," *IEEE Trans. Med. Imag.*, vol. 35, no. 1, pp. 273–281, Jan. 2016.

[4] I. F. Jones, M. C. Goodwin, I. D. Berranger, H. Zhou, and P. A. Farmer, "Application of anisotropic 3D reverse time migration to complex North Sea imaging," in *Proc. SEG Tech. Program Expanded Abstr.*, vol. 26, Jan. 2007, pp. 2140–2144.

[5] H. Yang, T. Li, N. Li, Z. He, and Q. H. Liu, "Time-gating-based time reversal imaging for impulse borehole radar in layered media," *IEEE Trans. Geosci. Remote Sens.*, vol. 54, no. 5, pp. 2695–2705, May 2016.

[6] C. J. Leuschen and R. G. Plumb, "A matched-filter-based reverse-time migration algorithm for ground-penetrating radar data," *IEEE Trans. Geosci. Remote Sens.*, vol. 39, no. 5, pp. 929–936, May 2001.

[7] C. P. Oden, M. H. Powers, D. L. Wright, and G. R. Olhoeft, "Improving GPR image resolution in lossy ground using dispersive migration," *IEEE Trans. Geosci. Remote Sens.*, vol. 45, no. 8, pp. 2492–2500, Aug. 2007.

[8] H. Liu, Z. Long, F. Han, G. Fang, and Q. H. Liu, "Frequency-domain reverse-time migration of ground penetrating radar based on layered medium Green's functions," *IEEE J. Sel. Topics Appl. Earth Observ. Remote Sens.*, vol. 11, no. 8, pp. 2957–2965, Aug. 2018.

[9] W. Dai, P. Fowler, and G. T. Schuster, "Multi-source least-squares reverse time migration," *Geophys. Prospecting*, vol. 60, no. 4, pp. 681–695, 2012.

[10] H. Zhou, M. Sato, and H. Liu, "Migration velocity analysis and prestack migration of common-transmitter GPR data," *IEEE Trans. Geosci. Remote Sens.*, vol. 43, no. 1, pp. 86–91, Jan. 2005.

[11] L. Lin-Lin, L. Si-Xin, F. Lei, and W. Jun-Jun, "Reverse time migration applied to GPR data based on full wave inversion," *Chin. J. Geophys.*, vol. 58, no. 9, pp. 3346–3355, Sep. 2015.

[12] C. P. Kao, J. Li, Y. Wang, H. Xing, and C. R. Liu, "Measurement of layer thickness and permittivity using a new multilayer model from GPR data," *IEEE Trans. Geosci. Remote Sens.*, vol. 45, no. 8, pp. 2463–2470, Aug. 2007.

[13] H. Liu and M. Sato, "*In situ* measurement of pavement thickness and dielectric permittivity by GPR using an antenna array," *NDT E Int.*, vol. 64, pp. 65–71, Jun. 2014.

[14] H. Liu *et al.*, "Reverse time migration of acoustic waves for imaging based defects detection for concrete and CFST structures," *Mech. Syst. Signal Process.*, vol. 117, pp. 210–220, Feb. 2019.

[15] S. Liu, L. Lei, L. Fu, and J. Wu, "Application of pre-stack reverse time migration based on FWI velocity estimation to ground penetrating radar data," *J. Appl. Geophys.*, vol. 107, pp. 1–7, Aug. 2014.

[16] G. A. Meles, J. Van der Kruk, S. A. Greenhalgh, J. R. Ernst, H. Maurer, and A. G. Green, "A new vector waveform inversion algorithm for simultaneous updating of conductivity and permittivity parameters from combination crosshole/borehole-to-surface GPR data," *IEEE Trans. Geosci. Remote Sens.*, vol. 48, no. 9, pp. 3391–3407, Sep. 2010.

[17] S. Lambot, E. C. Slob, I. V. D. Bosch, B. Stockbroeckx, and M. Vanclooster, "Modeling of ground-penetrating Radar for accurate characterization of subsurface electric properties," *IEEE Trans. Geosci. Remote Sens.*, vol. 42, no. 11, pp. 2555–2568, Nov. 2004.

[18] Z.-L. Huang and J. Zhang, "Determination of parameters of subsurface layers using GPR spectral inversion method," *IEEE Trans. Geosci. Remote Sens.*, vol. 52, no. 12, pp. 7527–7533, Dec. 2014.

[19] S. Maiti, S. K. Patra, and A. Bhattacharya, "A modified plane wave model for fast and accurate characterization of layered media," *IEEE Trans. Microw. Theory Techn.*, vol. 65, no. 9, pp. 3492–3502, Sep. 2017.

[20] S. Maiti, S. K. Patra, and A. Bhattacharya, "GPR modeling for rapid characterization of layered media," *Prog. Electromagn. Res. B*, vol. 63, pp. 217–232, Sep. 2015.

[21] B. Liang *et al.*, "A new inversion method based on distorted born iterative method for grounded electrical source airborne transient electromagnetics," *IEEE Trans. Geosci. Remote Sens.*, vol. 56, no. 2, pp. 877–887, Feb. 2018.

[22] F. Li, Q. H. Liu, and L.-P. Song, "Three-dimensional reconstruction of objects buried in layered media using Born and distorted Born iterative methods," *IEEE Geosci. Remote Sens. Lett.*, vol. 1, no. 2, pp. 107–111, Apr. 2004.

[23] C. Yu *et al.*, "Active microwave imaging II: 3-D system prototype and image reconstruction from experimental data," *IEEE Trans. Microw. Theory Techn.*, vol. 56, no. 4, pp. 991–1000, Apr. 2008.

[24] T. Zhu, J. M. Carcione, and M. A. B. Botelho, "Reverse time imaging of ground-penetrating radar and SH-seismic data including the effects of wave loss," *Geophysics*, vol. 81, no. 4, pp. H21–H32, Jul. 2016.